Proceedings of the ASME 2010 3rd Joint US-European Fluids Engineering Summer Meeting and 8th International Conference on Nanochannels, Microchannels, and Minichannels
FEDSM-ICNMM2010
August 1-5, 2010, Montreal, Canada

FEDSM-ICNMM2010-31277

MODEL DEVELOPMENT FOR FLUID STRUCTURE INTERACTION IN THE SLIP REGIME

Jennifer van Rij, Todd Harman, Tim Ameel
University of Utah
Salt Lake City, Utah, U.S.A.

ABSTRACT

While many microscale systems are subject to both rarefaction and fluid-structure-interaction (FSI) effects, most commercial algorithms cannot model both, if either, of these for general applications. This study modifies the momentum and thermal energy exchange models of an existing, continuum based, multifield, compressible, unsteady, Eulerian-Lagrangian FSI algorithm, such that the equivalent of first-order slip velocity and temperature jump boundary conditions are achieved at fluid-solid surfaces, which may move with time. Following the development and implementation of the slip flow momentum and energy exchange models, several basic configurations are considered and compared to established data to verify the resulting algorithm's capabilities.

NOMENCLATURE

A	cell fluid-solid surface area
A_c	fin cross sectional area
C	Stokes drag coefficient, $C_D\,Re/2$
C_D	drag coefficient, $F_D/(1/2)\rho_\infty u_\infty^2 D\,L$
c_p	specific heat at constant pressure
c_v	specific heat at constant volume
D	diameter or characteristic length
e	internal energy per unit mass
E	Young's modulus of elasticity, $9GK/(G+3K)$
$\boldsymbol{f}$	force per unit volume
F_D	drag force
G	shear modulus of elasticity
H_{rs}	thermal energy exchange coefficient
H_{rs}^{slip}	slip flow thermal energy exchange coefficient
h	heat transfer coefficient or channel height
I	moment of inertia
K	bulk modulus of elasticity
K_{rs}	momentum exchange coefficient
K_{rs}^{slip}	slip flow momentum exchange coefficient
k	thermal conductivity
Kn	Knudsen number, λ/D
L	length
Ma	Mach number, $Re\,Kn\sqrt{2/(\pi\gamma)}$
N	number of materials
Nu	Nusselt number, hD/k
P	pressure
Q	rotation matrix
q	thermal energy exchange rate per unit volume
q''	heat flux
R	gas constant
Re	Reynolds number, $\rho uD/\mu$
T	temperature
t	time
T_b	fin base temperature
$\boldsymbol{u}$	velocity vector
V	cell volume
$\boldsymbol{x}, \boldsymbol{y}, \boldsymbol{z}$	Cartesian coordinate directions
$\boldsymbol{x'}, \boldsymbol{y'}, \boldsymbol{z'}$	surface coordinate directions

Greek symbols

β_t	first-order temperature jump coefficient, $[(2-\sigma_t)/\sigma_t][2\gamma/(1+\gamma)][k/(c_p\mu)]$
β_v	first-order velocity slip coefficient, $(2-\sigma_v)/\sigma_v$
γ	ratio of specific heats, c_p/c_v
δ	fin deflection
θ	volume fraction
Θ	nondimensional temperature, $(T-T_\infty)/(T_b-T_\infty)$
λ	mean free path, $\mu/\rho\sqrt{2RT/\pi}$
μ	dynamic viscosity

ρ	density
$\boldsymbol{\sigma}$	stress
σ_t	thermal accommodation coefficient
σ_v	momentum accommodation coefficient
$\boldsymbol{\tau}$	shear stress
υ	specific volume
ϕ	rotation angle about the $\boldsymbol{z}$-axis
ψ	rotation angle about the $\boldsymbol{y}$-axis

Subscripts/Superscripts

-	before exchange contribution
+	after exchange contribution
0	initial value
∞	freestream value
i	inlet value
m	mean value
o	outlet value
r	material index
s	material index
w	wall value
x, y, z	Cartesian coordinate directions

BACKGROUND

Both rarefaction and fluid-structure-interaction (FSI) effects are significant for many microscale systems. Examples include micro valves, pumps, actuators, particulate flows, porous flows, two-phase flows, micro-air-vehicles, combustion, and heat exchangers. Rarefaction, typically quantified by the Knudsen number, *Kn*, which is the ratio of the fluid's mean free path to the characteristic length of the system, becomes significant for gaseous systems at the microscale. Rarefaction results in discontinuities of the velocity and temperature at fluid-solid boundaries, which, for the slip flow regime, $0.01 \le Kn \le 0.1$, are typically modeled with first-order slip velocity [1] and temperature jump [2] boundary conditions applied to the continuum based conservation of momentum and energy equations, respectively. FSI effects are significant for any system in which the thermal-fluid and structural dynamics are coupled, and consequently cannot be considered independently. As listed previously, there are already many microsystems that operate with FSI effects. However, while there are many microscale systems that are subject to both rarefaction and FSI effects, currently available computational algorithms do not, typically, have the ability or versatility required to accurately model these effects for a generic microsystem. As a result, there are few studies which have considered FSI for microsystems, and no widely available studies that have numerically considered both FSI and rarefaction in a microsystem.

The primary objective of this study is to modify the momentum and energy exchange models of an existing FSI algorithm, such that the equivalent of first-order slip velocity and temperature jump boundary conditions are achieved at fluid-solid boundaries, which may move and deform arbitrarily with time. The FSI algorithm that is utilized is a three-dimensional, unsteady, continuum based Eulerian-Lagrangian methodology in which fluids, modeled using ICE (implicit, continuous fluid, Eulerian) and solid materials, modeled with MPM (the material-point-method), may be modeled either independently or simultaneously. ICE is a finite volume, cell-centered, multimaterial, compressible, computational fluid dynamics (CFD) algorithm that originated at Los Alamos National Laboratory [3]. And, MPM is a particle based method for solid mechanics simulations [4]. The development and documentation of the MPM-ICE implementation currently utilized is given in [5, 6]. The MPM-ICE FSI algorithm utilizes a statistically averaged, or 'multifield,' approach, where, each material is continuously defined (ρ, $\boldsymbol{u}$, e, T, υ, θ, $\boldsymbol{\sigma}$, P), with some probability, over the entire computational domain. This approach differs from the, perhaps more common, separate domain methodology, in which, fluid and solid materials are defined separately, with only one material at each point, and interaction only occuring at material boundaries. The multifield approach is advantageous for the current application, because it tightly couples fluid-structure-interactions through the conservation equations, rather than explicitly though specified boundary conditions, which allows arbitrary distortion of material and material surfaces without explicit surface tracking, passing of boundary conditions, and excessive stability and convergence issues. Use of the MPM-ICE algorithm to evaluate rarefaction with FSI is further merited, as rarefaction effects have already been successfully studied utilizing the independent CFD portion of the algorithm, with slip boundary conditions implemented at the computational domain boundaries [7-9].

The multimaterial governing conservation equations employed by the MPM-ICE algorithm, are given in Eqs. (1) - (3) [6].

$$\frac{\partial \rho_r}{\partial t} + \nabla \cdot \left(\rho \boldsymbol{u}\right)_r = 0 \tag{1}$$

$$\frac{\partial \left(\rho \boldsymbol{u}\right)_r}{\partial t} + \nabla \cdot \left(\rho \boldsymbol{u}\boldsymbol{u}\right)_r = -\theta_r \nabla P + \nabla \cdot \left(\theta \boldsymbol{\tau}\right)_r + \sum_{s=1}^{N} \boldsymbol{f}_{rs} \tag{2}$$

$$\frac{\partial \left(\rho e\right)_r}{\partial t} + \nabla \cdot \left(\rho e \boldsymbol{u}\right)_r = - \frac{P\theta_r}{\upsilon_r}\frac{d\upsilon_r}{dt} + \left(\theta \boldsymbol{\tau}\right)_r : \nabla \boldsymbol{u}_r + \nabla \cdot \left(\theta k \nabla T\right)_r + \sum_{s=1}^{N} q_{rs} \tag{3}$$

Equations (1) - (3) are the ensemble average, r material, conservation of mass, momentum, and energy equations respectively, where there are N materials, θ_r is the r material volume fraction, and $\sum_{s=1}^{N} \boldsymbol{f}_{rs}$ and $\sum_{s=1}^{N} q_{rs}$ are models for the momentum and energy exchange between materials. Equations (1) - (3), along with individual material constitutive or equation-of-state models, and models for $\sum_{s=1}^{N} \boldsymbol{f}_{rs}$ and

$\sum_{s=1}^{N} q_{rs}$, form a complete system of equations. The detailed numerical solution strategy utilized by the MPM-ICE algorithm to solve this system of equations is presented in [6], and consequently will not be duplicated here.

The momentum and energy exchange models currently employed by the MPM-ICE algorithm to model FSI for standard continuum conditions ($Kn \approx 0$), are given in Eqs. (4) and (5).

$$\sum_{s=1}^{N} \boldsymbol{f}_{rs} = \sum_{s=1}^{N} K_{rs}\theta_r\theta_s\left(\boldsymbol{u}_s - \boldsymbol{u}_r\right) \tag{4}$$

$$\sum_{s=1}^{N} q_{rs} = \sum_{s=1}^{N} H_{rs}\theta_r\theta_s\left(T_s - T_r\right) \tag{5}$$

Eq. (4) models $\boldsymbol{f}_{rs}$, the force per unit volume on material r, due to interaction with material s, as a function of the scalar momentum exchange coefficient, K_{rs}, the material volume fractions, and the relative velocity between the two materials. Similarly, Eq. (5) models q_{rs}, the thermal energy exchange rate per unit volume for material r, due to interaction with material s, as a function of the scalar energy exchange coefficient, H_{rs}, the material volume fractions, and the temperature difference between the two materials. To avoid stability and convergence restrictions, the momentum and thermal energy exchange between materials is calculated within each cell implicitly, for each timestep, as shown in Eqs. (6) and (7).

$$\rho_r\boldsymbol{u}_r^{+} = \rho_r\boldsymbol{u}_r^{-} + \Delta t\sum_{s=1}^{N} K_{rs}\theta_r\theta_s\left(\boldsymbol{u}_s^{+} - \boldsymbol{u}_r^{+}\right) \tag{6}$$

$$\rho_r c_{v,r} T_r^{+} = \rho_r c_{v,r} T_r^{-} + \Delta t\sum_{s=1}^{N} H_{rs}\theta_r\theta_s\left(T_s^{+} - T_r^{+}\right) \tag{7}$$

The '-' and '+' superscripts in Eqs. (6) and (7) indicate values before and after the momentum and thermal energy exchange between materials, respectively, at the point in the timestep that the exchange contributions are calculated. It is assumed with the calculation of Eqs. (6) and (7) that the material masses, volume fractions, and specific heats are not modified by the momentum and energy exchange between materials. It is also necessary with the implementation of Eqs. (6) and (7) to specify momentum and energy exchange coefficients for all possible material pairs. However, K_{rs} must equal K_{sr}, and H_{rs} must equal H_{sr}, since the force, and heat transferred, from material r due to material s is equal and opposite the force, and heat transferred, from material s due to material r. And, $K_{rr} = H_{rr} = 0$, since the stress and heat flux within the same material are already accounted for with other terms of the momentum and energy conservation equations. A very large momentum transfer rate between materials r and s, specified by a large K_{rs} value, forces the relative velocity of the two materials to zero, consistent with a no-slip velocity boundary condition. Similarly, a large H_{rs} value produces a large thermal energy transfer rate between materials r and s, resulting in the equivalent of a thermal equilibrium boundary condition. In the current algorithm, K_{rs} and H_{rs} values are typically specified as arbitrarily large, constant, scalar quantities ($\sim 1\times 10^{15}$), which result in momentum and thermal energy transfer rates that are not directional relative to the fluid-solid surface, but produce the intended effect of conventional no-slip velocity and thermal equilibrium boundary conditions.

The objective of this study, is to modify the momentum and energy exchange models in the FSI algorithm, such that the equivalent of first-order slip velocity and temperature jump boundary conditions are achieved at fluid-solid surfaces for a rarified gas in the slip flow regime. To accomplish this, momentum and energy exchange models, which result in tangential slip velocity and temperature jump values that correspond to values predicted by the standard first-order slip boundary conditions [1, 2], are derived as a function of the level of rarefaction. Following the development and implementation of the slip flow momentum and energy exchange models, several basic configurations are considered and compared to established data to verify the resulting algorithm's capabilities. These verifications include: 1) velocity profiles of a rarified gas between parallel plates; 2) temperature profiles of a rarified gas between parallel plates; 3) drag coefficients, C_D, and Nusselt numbers, Nu, for low Reynolds number rarified flow around an infinite cylinder; and, 4) the transient, thermal/structural response of a damped-oscillatory three-dimensional finite cylinder subject to an impulsively started uniform, rarified flow.

SLIP FLOW MODIFICATIONS

Several modifications to the momentum and energy exchange models in the MPM-ICE FSI algorithm must be implemented to correctly model the momentum and energy exchange between a rarified gas and a moving, deforming solid surface. First, slip flow momentum and energy exchange coefficients must be derived, then the slip flow momentum and thermal energy exchange models must be applied at fluid-solid surfaces.

Slip flow momentum and thermal energy exchange coefficients

The tangential momentum exchange between a rarified gas, denoted as material r, and a solid material, material s, is described by the first-order slip velocity boundary condition, Eq. (8) [1]. To obtain the force per unit volume on the rarified gas due to interaction with the solid, $\boldsymbol{f}_{rs}$, the shear stress on the gas, $-\boldsymbol{\tau}$ from Eq. (8), is multiplied by the fluid-solid surface area in the cell, A, as well as the gas volume fraction, θ_r, and then divided by the cell volume, V, as shown in Eq. (9). For $\boldsymbol{f}_{rs}$ in Eq. (9) to be equivalent to the momentum exchange model utilized by the algorithm, Eq. (4), the slip flow tangential momentum exchange coefficient, K_{rs}^{slip}, must be that given by Eq. (10).

$$\boldsymbol{u}_r - \boldsymbol{u}_s = \frac{\beta_v\lambda_r}{\mu_r}\boldsymbol{\tau} \tag{8}$$

$$\boldsymbol{f}_{rs} = -\theta_r \boldsymbol{\tau}\left(\frac{A}{V}\right) = \left(\frac{\theta_r \mu_r}{\beta_v \lambda_r}\right)\left(\frac{A}{V}\right)\left(\boldsymbol{u}_s - \boldsymbol{u}_r\right) \tag{9}$$

$$K_{rs}^{slip} = \left(\frac{\mu_r}{\beta_v \lambda_r}\right)\left(\frac{A}{V}\right)\left(\frac{1}{\theta_s}\right) \tag{10}$$

In a similar fashion, using the first-order temperature jump boundary condition, Eq. (11) [2], and the energy exchange model, Eq. (5), the slip flow energy exchange coefficient is obtained in Eqs. (12) - (13).

$$T_r - T_s = -\frac{\beta_t \lambda_r}{k_r} q'' \tag{11}$$

$$q_{rs} = \theta_r q''\left(\frac{A}{V}\right) = \left(\frac{\theta_r k_r}{\beta_t \lambda_r}\right)\left(\frac{A}{V}\right)\left(T_s - T_r\right) \tag{12}$$

$$H_{rs}^{slip} = \left(\frac{k_r}{\beta_t \lambda_r}\right)\left(\frac{A}{V}\right)\left(\frac{1}{\theta_s}\right) \tag{13}$$

K_{rs}^{slip}, Eq. (10), and H_{rs}^{slip}, Eq. (13), are functions of the rarified gas viscosity, μ_r, thermal conductivity, k_r, and mean free path, λ_r; the solid material volume fraction, θ_s; the first-order slip velocity and temperature jump coefficients, β_v and β_t, respectively; and, the individual cell fluid-solid surface area, A, and volume, V. The cell fluid-solid surface area, A, is approximated according to Eq. (14), where Δx, Δy, and Δz are the cell dimensions in each coordinate direction, and y'_x, y'_y, and y'_z are components of the solid surface unit density gradient vector, as will be discussed further in the next section. Eq. (14) is not exact, but results in good estimates globally, as well as locally, if the surface is approximately parallel to any of the coordinate directions.

$$A = \frac{\Delta x \Delta y \Delta z}{y'_x \, \Delta x + y'_y \, \Delta y + y'_z \, \Delta z} \tag{14}$$

Values for μ_r, k_r, θ_s, and V are available within the unmodified algorithm, and values for β_v, β_t, and λ_r are calculated according to Eqs. (15) – (17), respectively [1, 2].

$$\beta_v = \frac{2 - \sigma_v}{\sigma_v} \tag{15}$$

$$\beta_t = \left(\frac{2 - \sigma_t}{\sigma_t}\right)\left(\frac{2\gamma_r}{1 + \gamma_r}\right)\left(\frac{k_r}{c_{p,r}\mu_r}\right) \tag{16}$$

$$\lambda_r = \frac{\mu_r}{\rho_r \sqrt{2 c_{\upsilon,r}(\gamma_r - 1) T_r / \pi}} \tag{17}$$

The momentum accommodation coefficient, σ_v in Eq. (15), and the thermal accommodation coefficient, σ_t in Eq. (16), must be measured experimentally. Values for σ_v and σ_t range from zero to one, where $\sigma_v = 0$ represents completely specular reflection, $\sigma_v = 1$ represents completely diffuse reflection, and $\sigma_t = 1$ corresponds to a perfect energy exchange. Experimentally measured values for σ_v and σ_t are, however, typically near unity, and consequently, are approximated as such for all calculations presented within this study. The rarified gas mean free path, λ_r, Eq. (17), is calculated for each cell of the computational domain, at the beginning of each timestep, as a function of μ_r, ρ_r, $c_{\upsilon,r}$, γ_r, and T_r.

Slip flow momentum and thermal energy exchange models

The original slip velocity and temperature jump boundary conditions given in Eqs. (8) and (11) [1, 2], were derived with the assumption that a rarified gas flow within the slip flow regime may be accurately approximated as a continuum everywhere except at the fluid-solid boundaries. To accurately model a flow within the slip flow regime the numerical algorithm must, likewise, produce continuous velocity and temperature fields everywhere except at the fluid-solid boundaries. Because each material is continuously defined in the MPM-ICE algorithm, this means that approximately equivalent temperatures for each material within the same cell must be obtained, and approximately equivalent velocities for each material within the same cell must be obtained, everywhere except at the fluid-solid boundaries, where discontinuities between the fluid and solid materials may occur. Therefore, the unmodified K_{rs} and H_{rs}, i.e. the arbitrary large, constant, scalar values that result in negligible velocity and temperature differences between materials within the same cell, are applied in the usual manner everywhere except at the fluid-solid surface. At the fluid-solid surface, slip flow momentum and energy exchange coefficients, K_{rs}^{slip} and H_{rs}^{slip}, respectively, must be applied. In the MPM algorithm, solid materials are modeled with material particles, typically eight particles per cell. As such, a surface is identified as a cell that has material particles of the specified solid material, but with less than eight particles. Because the surface may be in motion, and surfaces are not explicitly tracked, it is necessary with this approach to test each cell of the computational domain, with each timestep, to determine if it is a surface cell. If a surface cell is identified, K_{rs}^{slip} and H_{rs}^{slip}, as defined in Eqs. (10) and (13), are then calculated for that cell.

Temperature is a scalar quantity, and consequently, once a surface cell is identified and H_{rs}^{slip} is calculated, calculation of the thermal energy exchange between materials in that cell may precede using the usual algorithm, that is, the numerical implementation of Eq. (7), with H_{rs}^{slip} rather than H_{rs}. Velocity, however, is a vector quantity, and the momentum exchanged between materials must take place with respect to the coordinate system in which the velocity components are defined. In the unmodified algorithm, K_{rs} does not change with

direction, and so, the exchange of momentum between materials may be executed in the arbitrary global Cartesian coordinate system, $(\boldsymbol{x},\boldsymbol{y},\boldsymbol{z})$, in which, the velocities are originally defined. However, because K_{rs}^{slip} is only applicable in the fluid-solid surface tangential direction, while the standard no-slip K_{rs} must be applied in the fluid-solid surface normal direction, the momentum exchange between materials for slip flow must be executed in a coordinate system defined by the fluid-solid surface. The surface coordinate system $(\boldsymbol{x}',\boldsymbol{y}',\boldsymbol{z}')$, as illustrated by a hypothetical surface in Fig. 1, is defined by rotating $(\boldsymbol{x},\boldsymbol{y},\boldsymbol{z})$ by ϕ about $\boldsymbol{z}$, and then ψ about $\boldsymbol{y}$, such that $\boldsymbol{y}'$ is the outward unit normal direction of the solid surface. $\boldsymbol{y}'$ is calculated using the density gradient of the solid material particles within the surface cell, as shown in Eq. (18).

$$\boldsymbol{y}' = -\nabla\rho_s \big/ \left|\nabla\rho_s\right| \tag{18}$$

The material velocities in terms of $(\boldsymbol{x}',\boldsymbol{y}',\boldsymbol{z}')$ are obtained by applying the rotation matrix Q, given in Eq. (19), to $\boldsymbol{u}$ as shown in Eq. (20). By definition, Q is a real, orthogonal, special matrix ($Q^T = Q^{-1}$, $\det(Q) = 1$), in which the rows represent the $(\boldsymbol{x}',\boldsymbol{y}',\boldsymbol{z}')$ unit vectors as defined in the original $(\boldsymbol{x},\boldsymbol{y},\boldsymbol{z})$ system. Once the velocities are defined in terms of the coordinates, the $(\boldsymbol{x}',\boldsymbol{y}',\boldsymbol{z}')$ momentum exchange between materials is calculated for each surface coordinate direction, utilizing the numerical implementation of Eq. (6), with K_{rs}^{slip} in the $\boldsymbol{x}'$ and $\boldsymbol{z}'$ directions, and the no-slip K_{rs} in the $\boldsymbol{y}'$ direction. Following the exchange of momentum between materials in the $(\boldsymbol{x}',\boldsymbol{y}',\boldsymbol{z}')$ system, the material velocities are then returned to the $(\boldsymbol{x},\boldsymbol{y},\boldsymbol{z})$ description utilizing Q^T as shown in Eq. (21).

$$Q = \begin{bmatrix} x'_x & x'_y & x'_z \\ y'_x & y'_y & y'_z \\ z'_x & z'_y & z'_z \end{bmatrix} = \begin{bmatrix} \cos\phi\cos\psi & -\sin\phi & \cos\phi\sin\psi \\ \sin\phi\cos\psi & \cos\phi & \sin\phi\sin\psi \\ -\sin\psi & 0 & \cos\psi \end{bmatrix} \rightarrow$$
$$\begin{bmatrix} \dfrac{y'_y\, y'_x}{\sqrt{1-y'^2_y}} & -\sqrt{1-y'^2_y} & \dfrac{y'_y\, y'_z}{\sqrt{1-y'^2_y}} \\ y'_x & y'_y & y'_z \\ \dfrac{-y'_z}{\sqrt{1-y'^2_y}} & 0 & \dfrac{y'_x}{\sqrt{1-y'^2_y}} \end{bmatrix} \tag{19}$$

$$\sum_{s=1}^{N} \boldsymbol{u}'^{-}_s = \sum_{s=1}^{N} Q\boldsymbol{u}^{-}_s \tag{20}$$

$$\sum_{s=1}^{N} \boldsymbol{u}^{+}_s = \sum_{s=1}^{N} Q^T \boldsymbol{u}'^{+}_s \tag{21}$$

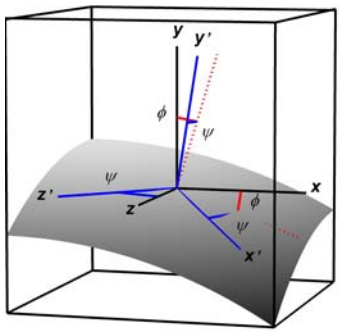

Fig. 1. Global and surface coordinate systems.

NUMERICAL RESULTS

To verify the methodology and implementation of the modifications described for the slip flow momentum and energy exchange models, several basic configurations, as outlined previously, are evaluated. For each configuration, the numerical results are substantiated with grid convergence and order-of-accuracy studies, as well as comparisons to previously established data.

Pressure driven flow between parallel plates

A pressure driven, fully developed, steady state, Newtonian, rarified ideal gas flow between parallel plates with constant properties and negligible inertial forces, as specified in Fig. 2(a), is modeled to verify the accuracy and implementation of the slip flow momentum exchange modifications in the MPM-ICE algorithm. The analytic velocity solution used to verify the numerical data, Eq. (22), is obtained by integrating the momentum equation, $\mu\left(\partial^2 u/\partial y^2\right) = dP/dx$, twice, and applying the slip velocity boundary condition at the wall, $u\big|_{y=0} = \beta_v \lambda \left(\partial u/\partial y\right)_{y=0}$, and symmetry at the midplane, $\left(\partial u/\partial y\right)_{y=h/2} = 0$, and then normalizing by the resulting mean velocity, u_m.

$$\frac{u(y/h)}{u_m} = \frac{6\left(y/h - y^2/h^2 + 2\beta_v Kn\right)}{1 + 12\beta_v Kn} \tag{22}$$

The pressure driven flow configuration is evaluated for $Kn_m = 0.0000$, 0.0564, and 0.1128, and grid resolutions of $\Delta x = \Delta y = h/10$, $h/20$, and $h/40$. The numerical data for $\Delta x = h/40$ are compared to Eq. (22), as well as the Boltzmann equation solution presented by [10] for comparable conditions, at steady-state ($t = 0.1\mu s$) in Figs. 2(b) and 2(c), for $Kn_m = 0.0564$ and 0.1128, respectively. The numerical results obtained, not all of which are presented here, indicate that the modified slip flow momentum exchange model accurately represents slip velocity boundary conditions compared to first-order boundary conditions, converges with the same order-of-accuracy as the original algorithm (~1.0), and conserves the exchanged momentum.

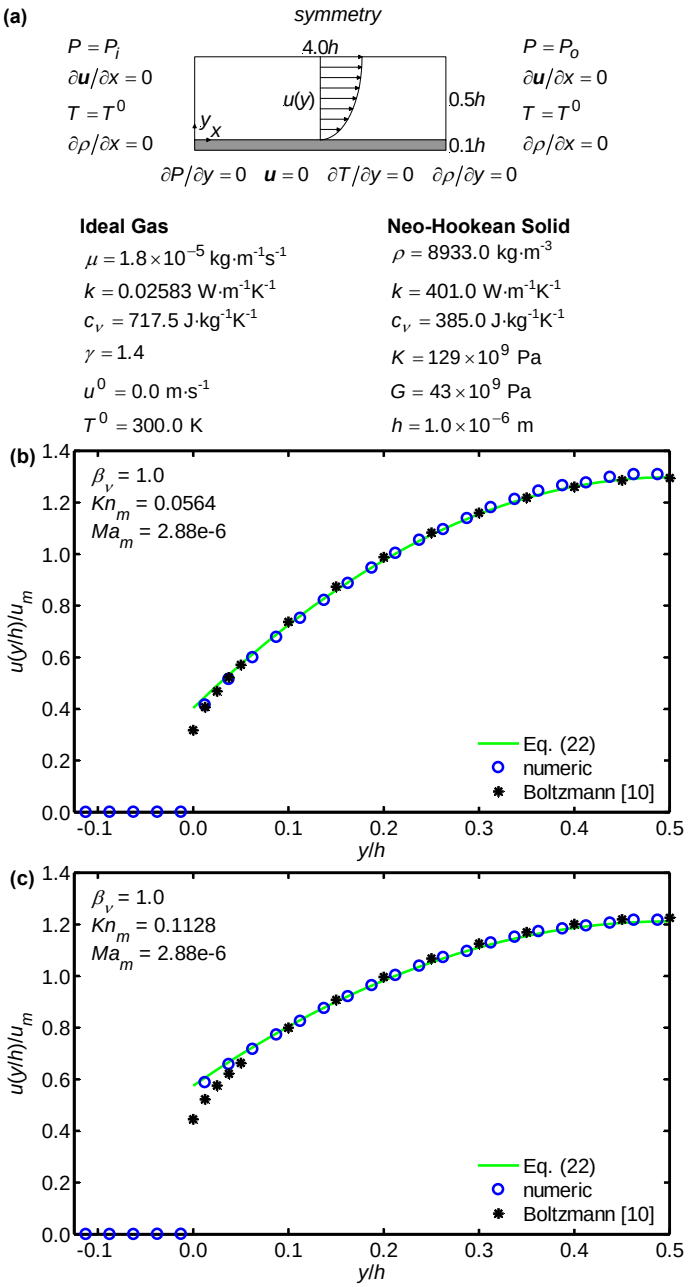

Fig. 2. Steady state ($t = 0.1\mu s$) pressure driven flow between parallel plates: (a) problem specification, (b) velocity profile, $Kn_m = 0.0564$, (c) velocity profile, $Kn_m = 0.1128$.

Thermal conduction between parallel plates

The steady state thermal conduction of a stationary, constant property, rarified ideal gas between two parallel plates of different temperatures, as specified in Fig. 3(a), is modeled with the MPM-ICE algorithm to verify the accuracy and implementation of the slip flow thermal energy exchange modifications. The analytic temperature profile used to verify the numerical data, Eq. (23), is derived by integrating the energy equation, $\partial^2 T/\partial y^2 = 0$, twice, and applying temperature jump boundary conditions at each wall, $T\big|_{y=0} = T_w - \Delta T + \beta_t \lambda (\partial T/\partial y)_{y=0}$ and $T\big|_{y=0} = T_w + \Delta T - \beta_t \lambda (\partial T/\partial y)_{y=h}$.

$$\frac{T(y/h) - T_w}{\Delta T} = \frac{-1 + 2(y/h)}{1 + 4\beta_t Kn} \tag{23}$$

The thermal conduction configuration is evaluated for $Kn_m = 0.0000$, 0.0564, and 0.1128, and grid resolutions of $\Delta x = \Delta y = h/10$, $h/20$, and $h/40$. The numerical data for $\Delta x = \Delta y = h/40$ are compared to Eq. (23) at steady-state ($t = 0.1\mu s$) in Fig. 3(b) for the parameters specified. The numerical results obtained, not all of which are presented here, indicate that the modified slip flow energy exchange model accurately represents temperature jump when compared to first-order temperature jump boundary conditions, converges with the same order-of-accuracy as the original algorithm, ~0.8, and conserves the exchanged energy.

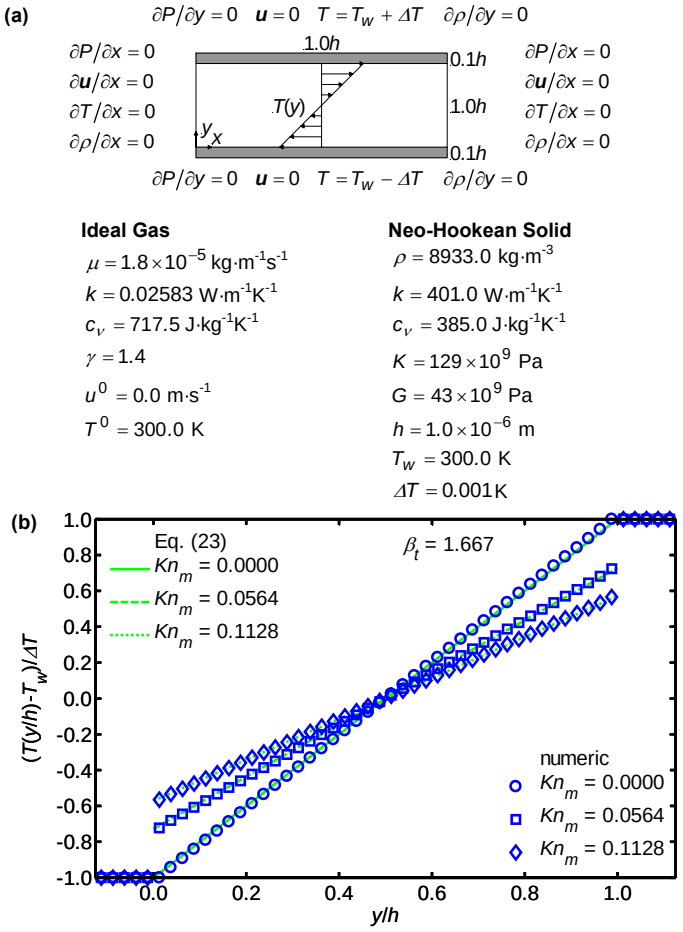

Fig. 3. Steady state ($t = 0.1\mu s$) thermal conduction between parallel plates: (a) problem specification, (b) temperature profiles, $Kn_m = 0.0000$, $Kn_m = 0.0564$, $Kn_m = 0.1128$.

Low Reynolds number, infinite cylinder C_D and Nu

To verify that the MPM-ICE algorithm, with the slip flow momentum and energy exchange modifications, accurately represents a rarified gas flow for a more complex geometry than the two previous configurations, flow around an infinite circular cylinder is evaluated. C_D and *Nu* are evaluated at very low *Re* in this study for several reasons. Most significantly, typical microfluidic system *Re* are very small, due to the small length scales. Additionally, the symmetry present at low *Re* may be utilized to reduce the computational problem size. Also, without flow separation, effects due to rarefaction only should be more evident. And, furthermore, some slip flow C_D and *Nu* data are available for comparison to numerical results at low *Re*, while none exists at higher *Re*.

The numerical problem specification and flow parameters utilized to model flow around an infinite cylinder are presented in Fig. 4(a). To numerically approximate an unconfined cylinder at very low *Re*, a large computational domain size and locally one-dimensional inviscid (LODI) boundary conditions, as described in [11], are used. To reduce the size of the resulting computational problem a multilevel stationary grid is used. Three different grids are considered, $\Delta x = \Delta y = D/4$, $D/8$, and $D/16$ are used immediately around the cylinder; from 2.5*D* to 5*D* away from the cylinder center, the grid size is double the given values; and, from 5D away from the cylinder center to the edge of the computational domain, the grid size is four times the given value.

The numerical C_D per unit length are obtained utilizing the standard definition, $C_D = F_D \big/ (1/2)\rho_\infty u_\infty^2 D$, where (1/2) F_D is first computed via an integral *x*-momentum analysis around the symmetric cylinder. Similarly, the numerical *Nu* are calculated with the usual definition, $Nu = \bar{q}''_{cyl} D \big/ k_r (T_s - T_\infty)$, where $\bar{q}''_{cyl}(\pi D/2)$, one-half of the thermal energy exchange rate per unit length due to the cylinder, is first obtained via an integral thermal energy analysis around the symmetric cylinder. The resulting steady state (t = 180μs) C_D and *Nu* for the highest grid resolution are plotted and compared to reference values in Figs. 4(b) and 4(c), respectively.

The numerically determined infinite cylinder C_D reported in Fig. 4(b) for $Kn = 0.0$, is within 8.0% of the reference value at $Re = 1.37$, and within 20% of the reference values at $Re = 0.1$ [12, 13]. The larger difference at $Re = 0.1$, is because the reference C_D values are for an unconfined cylinder, which cannot be accurately numerically simulated, particular at low *Re*. The effect of *Kn* on the numerically determined cylinder C_D is comparable to, although less than, the analytically predicted effect of *Kn* on sphere C_D [14]. The numerically determined cylinder C_D is roughly 1-2% less for $Kn = 0.042$, and 2-3% less for $Kn = 0.076$.

The numerical *Nu* for $Kn = 0.0$, are within 8% of the correlation values of [17]. The effect of rarefaction on the numerically determined *Nu* at $\mathrm{Re} \sim 0.1$, is roughly a 3% decrease at $Kn = 0.042$, and a 5% decrease at $Kn = 0.076$, which is somewhat less than expected based on the experimental values [18].

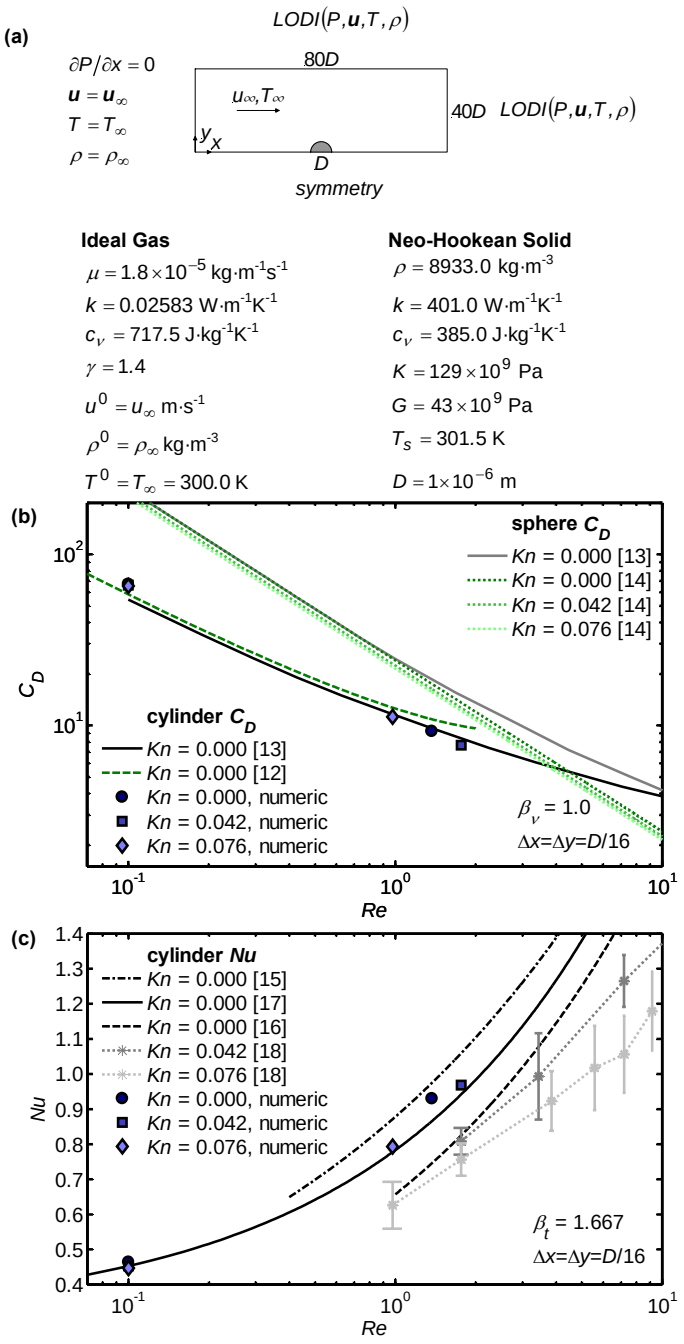

Fig. 4. Steady state (t = 180μs) low Reynolds number, infinite cylinder C_D and *Nu*: (a) problem specification, (b) C_D, (c) *Nu*.

The numerical slip flow *Nu* at $Re \approx 1$ are likely higher than the experimental slip flow *Nu*, due, in part, to the approximation of $\sigma_t = 1$. Experimentally measured σ_t are often near 1, but may be any value between 0 and 1, and a value of σ_t less than 1 would result in an increase in the temperature jump at the surface, and decrease in *Nu*. Overall, the agreement between the numerically determined C_D and *Nu* with the reference values and trends validate that the MPM-ICE algorithm, with the slip flow

momentum and energy exchange modifications, adequately represents the thermal/hydrodynamic flow behavior of a rarified gas around an infinite circular cylinder. The average grid resolution order-of-accuracy is ~1.0 for C_D and ~0.6 for *Nu*.

Unsteady slip flow fluid-structure-interaction

To verify that the algorithm is capable of accurately predicting unsteady fluid-structure-interaction with a rarified flow, the thermal/structural response of a damped-oscillatory three-dimensional cylindrical fin, subject to an impulsively started uniform, rarified flow, as illustrated in Fig. 5(a), is evaluated. This particular configuration is evaluated because there are several similar microscale applications, including, atomic force microscope measurements, heat exchangers, and bio-sensors and actuators. In this evaluation, the fin initially has zero displacement, $\delta(y,0)=0$, zero velocity, $\partial\delta(y,0)/\partial t=0$, and a uniform temperature equal to the constant fin base temperature, $T(y,0)=T(0,t)=T_b$. The rarified gas initially has a uniform velocity, u_∞, and a uniform temperature, T_∞, that is less than the fin base temperature. As the system is set in motion, the sudden fluid force on the fin results in its displacement and subsequent damped oscillation while it simultaneously transfers heat to the fluid.

To verify the numerical simulation of this system, comparisons to analytic solutions are necessary. The governing equation for beam vibration, the Euler-Bernoulli equation [19], may be solved with the force of the fluid modeled as a Stokes drag force, $F_D(y,t)/L = C\mu(u_\infty - \partial\delta(y,t)/\partial t)$, which is accurate for very low *Re* flow. The Stokes drag coefficient, *C*, is related to the typical drag coefficient as $C_D = 2C/Re$. The Euler-Bernoulli equation, boundary conditions, initial conditions, and resulting analytic fin displacement solution, $\delta(y,t)$, as obtain by the standard solution methods of separation-of-variables and orthogonality, are summarized in Table 1. The governing energy equation for the fin, boundary conditions, initial conditions, and resulting analytic transient temperature distribution, obtained, again, by the standard solution methods of separation-of-variables and orthogonality, are summarized in Table 2. To derive the unsteady, normalized, analytic temperature distribution, $\Theta(y,t)$, it is assumed that the transient fin temperature varies only axially and that the convective heat transfer coefficient, *h*, is uniform and constant. In reality, however, *h* varies both spatially and temporally, and the fin cross sectional temperature will also vary slightly. Consequently, the analytic $\Theta(y,t)$ solution presented in Table 2, is only expected to provide an approximate comparison to the numerical data.

For the configuration illustrated in Fig. 5(a) both continuum flow, $Kn = 0$, and rarified flow, $Kn = 0.042$, are evaluated for both a flexible ($E = 5\times10^6$ Pa) and rigid fin. This results in four evaluation cases: 1) $Kn = 0$, $E = 5\times10^6$; 2) $Kn = 0.042$, $E = 5\times10^6$; 3) $Kn = 0$, rigid; 4) $Kn = 0.042$, rigid - each of which is evaluated at three different grid resolutions, $\Delta x = \Delta y = \Delta z = D/1$, $D/2$, and $D/4$. The transient numerical solution is obtained for $0 < t < 180\mu s$. $\delta(y,t)/D$, for the highest grid resolution, is presented and compared to the analytic solution in Fig. 5(b). All of the parameters required to calculate the analytic $\delta(y,t)/D$ (Table 1), are specified in Fig. 5(a), except, *C* (= $ReC_D/2$), which is unknown. Therefore, for cases 1 and 2, which are the flexible fins, the C_D that results in the smallest L_2 norm error between the analytic and numeric $\delta(y,t)/D$ is utilized to obtain the analytic solution, as reported in Fig. 5(b).

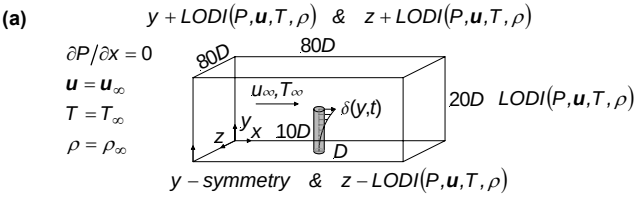

Ideal Gas

$\mu = 1.8\times10^{-5}$ kg·m^{-1}s^{-1}
$k = 0.02583$ W·m^{-1}K^{-1}
$c_v = 717.5$ J·kg^{-1}K^{-1}
$\gamma = 1.4$
$u^0 = u_\infty = 0.983$ m·s^{-1}
$\rho^0 = \rho_\infty = 1.831$ kg·m^{-3}
$T^0 = T_\infty = 300.0$ K

Neo-Hookean Solid

$\rho = 1000.0$ kg·m^{-3}
$k = 0.16$ W·m^{-1}K^{-1}
$c_v = 2010.0$ J·kg^{-1}K^{-1}
$K = 5.56\times10^6$ Pa
$G = 1.85\times10^6$ Pa
$D = 1\times10^{-6}$ m
$T^0 = T_b = 301.5$ K
$u^0 = 0.0$ m·s^{-1}

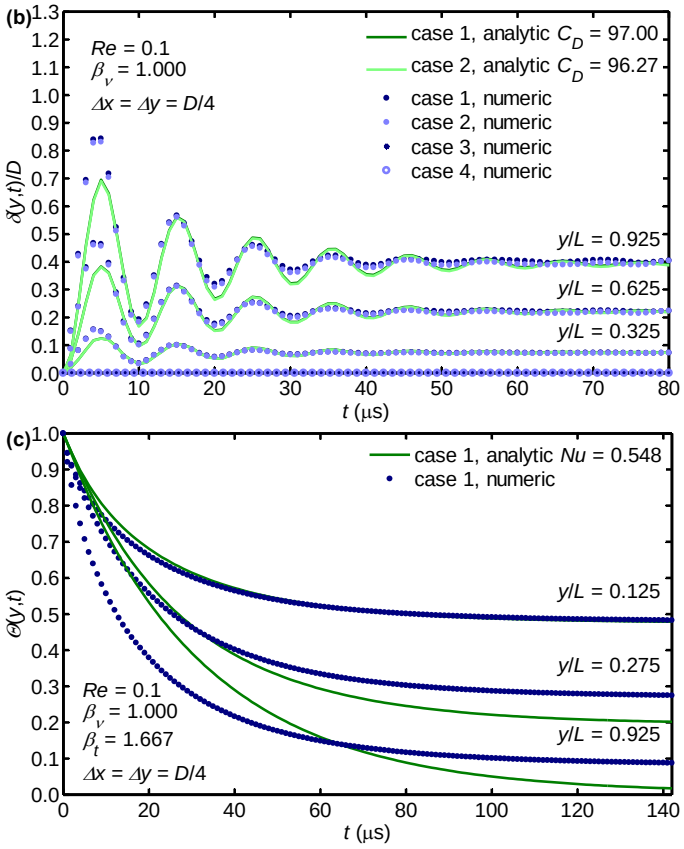

Fig. 5. Unsteady slip flow fluid-structure-interaction: (a) problem specification, (b) $\delta(y,t)/D$, (c) $\Theta(y,t)$.

Table 1. Analytic solution for transient fin displacement.

Governing Equation

$$\partial^2\delta(y,t)/\partial t^2 + (C\mu/\rho_s A_c)\partial\delta(y,t)/\partial t + (EI/\rho_s A_c)\partial^4\delta(y,t)/\partial y^4 = C\mu u_\infty/\rho_s A_c$$

Boundary Conditions

$$\delta(0,t) = 0$$
$$\partial\delta(0,t)/\partial y = 0$$
$$\partial^2\delta(L,t)/\partial y^2 = 0$$
$$\partial^3\delta(L,t)/\partial y^3 = 0$$

Initial Conditions

$$\delta(y,0) = 0$$
$$\partial\delta(y,0)/\partial t = 0$$

Solution

$$\delta(y,t) = \delta_p(y) + \sum_{n=1}^{\infty} Y_n(y) A_n \exp(-\varsigma_n\omega_n t)\left[\cos(\omega_{d,n}t) + (\varsigma_n\omega_n/\omega_{d,n})\sin(\omega_{d,n}t)\right]$$

$$\delta_p(y) = \left(C\mu u_\infty y^2/24EI\right)\left(6L^2 - 4Ly + y^2\right)$$

$$Y_n(y) = \cosh(\beta_n y) - \cos(\beta_n y) - \sigma_n \sinh(\beta_n y) + \sigma_n \sin(\beta_n y)$$

$$\sigma_n = \left[\sinh(\beta_n L) - \sin(\beta_n L)\right]/\left[\cosh(\beta_n L) + \cos(\beta_n L)\right]$$

$$\cosh(\beta_n L)\cos(\beta_n L) = -1$$

$$A_n = -\int_0^L \delta_p(y) Y_n(y)dy \Big/ \int_0^L Y_n^2(y)dy$$

$$\omega_n = \beta_n^2\sqrt{EI/\rho_s A_c}$$

$$\varsigma_n = \left(C\mu/2\rho_s A_c\beta_n^2\right)\sqrt{\rho_s A_c/EI}$$

$$\omega_{d,n} = \omega_n\sqrt{1-\varsigma_n^2}$$

n	$\beta_n L$	$\frac{A_n}{C\mu u_\infty L^4/24EI}$
1	1.8751	$-1.5201\cdot10^{0}$
2	4.6941	$-2.1450\cdot10^{-2}$
3	7.8548	$-1.6041\cdot10^{-3}$
4	10.9955	$-2.9866\cdot10^{-4}$
5	14.1372	$-8.5002\cdot10^{-5}$

Table 2. Analytic solution for transient fin temperature distribution.

Governing Equation

$$\partial^2 T(y,t)/\partial y^2 - m^2\left[T(y,t) - T_\infty\right] = \left(\rho_s c_{v,s}/k_s\right)\partial T(y,t)/\partial t$$

$$m^2 = 4h/Dk_s$$

Boundary Conditions

$$T(0,t) = T_b$$
$$T(L,t) - T_\infty = -(k/h)\partial T(L,t)/\partial y\big|_{y=L}$$

Initial Conditions

$$T(y,0) = T_b$$

Solution

$$\frac{T(y,t)-T_\infty}{T_b-T_\infty} = \Theta(y,t) = \Theta_p(y) + \sum_{n=1}^{\infty} C_n \exp\left[-\left(\frac{k_s t}{\rho_s c_{v,s}}\right)\left(m^2 + \Lambda_n^2\right)\right]\sin(\Lambda_n y)$$

$$\Theta_p(y) = \frac{\cosh\left[m(L-y)\right] + (h/mk_s)\sinh\left[m(L-y)\right]}{\cosh(mL) + (h/mk_s)\sinh(mL)}$$

$$\tan(\Lambda_n L) = -(k_s/hL)(\Lambda_n L)$$

$$C_n = \left(\frac{4\Lambda_n}{2\Lambda_n L - \sin(2\Lambda_n L)}\right)\left\{\frac{1-\cos(\Lambda_n L)}{\Lambda_n} - \frac{\Lambda_n - \left[\Lambda_n\cos(\Lambda_n L) + (h/k_s)\sin(\Lambda_n L)\right]/\left[\cosh(mL) + (h/mk_s)\sinh(mL)\right]}{m^2 + \Lambda_n^2}\right\}$$

Because C_D is calculated from the fin deflection, no C_D is obtained, for the rigid cases. The expected C_D for an unconfined, infinite cylinder, at $Re = 0.1$ is 58.39 [12]. The numerical finite, cylindrical fin C_D obtained for cases 1 and 2, are larger than this, due to effects of flow around the tip of the fin, the course grid resolution, and the proximity of the computational boundaries to the fin. C_D for $Kn = 0.042$ are approximately 1% less than C_D for $Kn = 0.0$. Although this reduction in C_D due to rarefaction is slight, it is consistent in magnitude with the reduction in C_D due to rarefaction for the infinite cylinder presented previously.

All of the parameters required to calculate the analytic $\Theta(y,t)$ (Table 2), are specified in Fig. 5(a), except, h (= Nuk_f/D), which is unknown. Consequently, the Nu that results in the minimum L_2 norm error between the analytic and numeric $\Theta(y,t)$, is utilized to obtain the analytic solution. The numeric and analytic $\Theta(y,t)$ for case 1 are compared in Fig. 5(c) for the highest grid resolution. Only data for case 1 are presented since the data for each of the other three cases are visually very similar. Numeric and analytic $\Theta(y,t)$ in Fig. 5(c) are comparable, but not identical, since h in the simulation is not uniform or constant, as assumed in the analytic solution. Re for these data are 0.1, the expected steady state Nu for an unconfined, infinite cylinder, at $Re = 0.1$ is 0.45 [17]. Although the numerical Nu data are not thermally steady state, the fin is finite in length, and confined by computational boundaries, all of the numerically computed Nu are comparable. For the four cases, rarefaction effects decrease Nu by ~2%, and the effect of the flexible fin's motion increases Nu by ~1%.

The numerical results, not all of which are presented here, indicate that the solution converges with approximately first-order numerical accuracy. In addition, the algorithm with the slip flow modifications, qualitatively predicts the unsteady fluid-structure-interaction of a damped-oscillatory three-dimensional cylindrical fin as compared to the analytically predicted displacement and temperature solutions.

SUMMARY

This study modifies the momentum and thermal energy exchange models of an existing, continuum based, multifield, compressible, unsteady, Eulerian-Lagrangian FSI algorithm, such that, for a rarified gas in the slip flow regime, the equivalent of first-order slip velocity and temperature jump boundary conditions are achieved at fluid-solid surfaces, which may move and deform with time. The momentum and thermal energy exchange models are modified by utilizing slip flow momentum and energy exchange coefficients that are derived as a function of the level of rarefaction from the original first-order slip velocity and temperature jump boundary conditions. The momentum and energy exchange models with the slip flow momentum and energy exchange coefficients are then applied at fluid-solid surfaces such that momentum is exchanged between the rarified gas and the solid material in the fluid-solid surface normal and tangential coordinate directions, rather than arbitrary global coordinates, and slip flow in the surface tangential direction, is realized.

Following the development and implementation of the slip flow momentum and energy exchange modifications, several basic configurations are considered to verify the resulting algorithm's capabilities. The configurations include the velocity profiles of a rarified gas between parallel plates,

temperature profiles of a rarified gas between parallel plates, drag coefficients, C_D, and Nusselt numbers, Nu, for low Reynolds number rarified flow around an infinite cylinder, and the transient, thermal/structural response of a damped-oscillatory three-dimensional finite cylinder subject to an impulsively started uniform, rarified flow. For each configuration, the numerical results are evaluated with grid convergence and order-of-accuracy studies, as well as comparison to analytical, experimental, or previously established reference data. Results of these evaluations indicate that 1) the slip flow momentum and energy exchange models conserve exchanged momentum and energy, respectively, and 2) that with these models, the algorithm is capable of modeling steady and unsteady fluid-structure-interaction with rarefaction effects, with accuracy approximately equivalent to the first-order slip velocity and temperature jump boundary conditions.

There are many microscale systems for which both rarefaction and fluid-structure-interaction effects are significant. Based on the modifications and verifications presented in this study, it is expected that the MPM-ICE algorithm, with the slip flow momentum and energy exchange modifications, has the unique ability to accurately model and evaluate these systems.

REFERENCES

[1] J.C. Maxwell, On stresses in rarified gases arising from inequalities of temperature, Phil. Trans. R. Soc. Lond. 170 (1879) 231-256.

[2] M. Smoluchowski, Ueber wärmeleitung in verdünnten gasen, Annal. Phys. Chem. 64 (1898) 101-130.

[3] B.A. Kashiwa, N.T. Padial, R.M. Rauenzahn, W.B. VanderHeyden, A Cell-Centered ICE Method for Multiphase Flow Simulations, Los Alamos National Laboratory Technical Report LA-UR-93-3922, 1993.

[4] D. Sulsky, Z. Shi-Jian, H.L. Schreyer, Application of a particle-in-cell method to solid mechanics, Comput. Phys. Comm. 87 (1-2) (1995) 236-252.

[5] B.A. Kashiwa, A Multifield Model and Method for Fluid-Structure Interaction Dynamics, Los Alamos National Laboratory Technical Report LA-UR-01-1136, 2001.

[6] J.E. Guilkey, T.B. Harman, B. Banerjee, An Eulerian–Lagrangian approach for simulating explosions of energetic devices, Comput. Struct. 85 (2007) 660-674.

[7] J. van Rij, T. Harman, T. Ameel, The effect of creep flow on two-dimensional isoflux microchannels, Int. J. Thermal Sci. 46 (11) (2007) 1095-1103.

[8] J. van Rij, T. Ameel, T. Harman, The effect of viscous dissipation and rarefaction on rectangular microchannel convective heat transfer, Int. J. Thermal Sci. 48 (2) (2009) 271-281.

[9] J. van Rij, T. Ameel, T. Harman, An evaluation of secondary effects on microchannel frictional and convective heat transfer characteristics, Int. J. Heat Mass Transfer 52 (11-12) (2009) 2792-2801.

[10] T. Ohwada, Y. Sone, K. Aoki, Numerical analysis of the Poiseuille and thermal transpiration flows between two parallel plates on the basis of the Boltzmann equation for hard-sphere molecules, Phys. Fluids 1 (12) (1989) 2042-2049.

[11] J.C. Sutherland, C.A. Kennedy, Improved boundary conditions for viscous, reacting, compressible flows, J. Comput. Phys. 191 (2003) 502-524.

[12] Sir. H. Lamb, Hydrodynamics, University Press, Cambridge, 1932.

[13] H. Schlichting, K. Gersten, Boundary-layer theory, eight ed., Springer, New York, 2000.

[14] R.W. Barber, Y. Sun, X.J. Gu, D.R. Emerson, Isothermal slip flow over curved surfaces, Vacuum, 76 (1) (2004) 73-81.

[15] R. Hilpert, "Wärmeabgabe von geheizten Drähten und Rohren im Luftstrom," Forsch. Geb. Ingenieurwes. 4 (5) (1933) 215-224.

[16] A. Zhukauskas, Heat Transfer from Tubes in Cross Flow, in: J.P. Hartnett, T.F. Irvine, Jr. (Eds.), Advances in Heat Transfer, vol. 8, Academic Press, N.Y., 1972.

[17] S.W. Churchill, M. Bernstein, Correlating equation for forced convection from gases and liquid to a circular cylinder in crossflow, J. Heat Tran. 99 (2) (1977) 300-306.

[18] L.V. Baldwin, Slip-flow heat transfer from cylinders in subsonic airstreams, Lewis Flight Propulsion Laboratory, National Advisory Committee for Aeronautics Technical Note NACA-TN-4369, 1958.

[19] D.J. Inman, Engineering vibration, Prentice Hall, Englewood Cliffs, N.J., 1994.